(Received 19 December 2024, Accepted 17 June 2025, Scheduled 27 July 2025)

Spatiotemporal Encoding Metasurface Based on BPSO-GA Optimization Method

(*Invited Paper*)

Xueyan Wang[1, 2, †], Rui Xi[1, 2, 3, *, †], Xinan Hou[1, 2, †], Huanran Qiu[2, 3], Zihui Liu[2], Dexiao Xia[3], Xiaokui Kang[2], Shiyun Ma[2], Yuanhao Zhang[2], Long Li[3], Lan Lan[1, *], and Guisheng Liao[1, *]

[1] *National Key Laboratory of Radar Signal Processing, Xidian University, Xi'an 710071, China*
[2] *Hangzhou Institute of Technology, Xidian University, Hangzhou 311231, China*
[3] *Key Laboratory of High-Speed Circuit Design and EMC of Ministry of Education School of Electronic Engineering, Xidian University, Xi'an 710071, China*

ABSTRACT: This paper introduces a spatiotemporal encoding method based on metasurface that enables precise frequency control and functional switching of radiation beams. The metasurface is configured with subarrays, and each subarray is designed to reflect a specific frequency, thereby achieving unique multi-target signal diversity. By manipulating the spatiotemporal phase of subarray elements, the metasurface can generate far-field radiation patterns with beam characteristics of consistent beam angle at different distances, or beam characteristics of consistent distance with different beam angles. The radiation energy distribution at harmonic frequencies is verified to remain symmetry under various 1 bit spatiotemporal encoding matrices, while the symmetry is verified to be broken by 2 bit spatiotemporal encoding matrices. An optimization method of genetic algorithm (GA) improved binary particle swarm optimization (BPSO) based on 2-bit-coding is thus developed to optimize the spatiotemporal modulation of the metasurface subarray. The GA with the advantage of crossover mutation operation is utilized to enhance population diversity and thus prevent the algorithm from falling into local optimality with improved search efficiency in high-dimensional discrete space. The optimization method balances different performance parameters and can achieve unique multi-target signal diversity, thereby improving the metasurface's ability to dynamically control and manipulate energy distribution. Using a 1-bit cross-switching mechanism with a duty cycle of 50%, the metasurface can suppress specific harmonic frequencies on the line of sight to less than -60 dBi while keeping the sidelobes below -20 dBi. The technology can precisely control the harmonic energy distribution while allowing beam at specific harmonic frequencies to be absorbed or reflected, which realize advanced breakthrough for effective selective stealth. Simulation results validate the proposed digital encoding optimization method, and the mainlobe gain of the metasurface harmonics is obtained to be more than 20 dBi. This paper algorithmically improves the beam gain of the metasurface and explores the versatile applications of spatiotemporal metasurfaces.

1. INTRODUCTION

Metasurface refers to artificial arranged subwavelength units according to certain criteria [1, 2]. Due to its specific electromagnetic control with ultra-thin thickness, low loss, and easy manufacturing, attention has been attracted from the scientific and engineering communities. Due to its feasibility, it provides great freedom to control the energy intensity at harmonic frequencies with phase and polarization manipulation. Great application potential has been shown in the fields of stealth [3, 4], low scattering cross section [5], and high-performance antenna [6]. Metamaterial perfect absorber can reduce radar cross section (RCS) by absorbing incident electromagnetic waves [7]. A method to reduce the radar cross section was proposed by using energy cancellation between the metasurface and metal ground [8]. Specially, metamaterial invisibility has attracted much attention with the famous "invisibility cloak" bending electromagnetic waves directed at the target to bypass the target [9]. Deep learning method was introduced into the design of metasurface stealth to adaptively modulate the incident wave [10]. Stealth solution was studied and demonstrated with target stealth effectively achieved [11, 12]. A three-dimensional metasurface stealth cloak based on microwave frequency full polarization and arbitrary shape was proposed with the radar scattering energy measured at vertical and oblique incidence [13]. A method combining singular transformation and transformation invariant metamaterials was proposed to achieve stealth and target's RCS reduction [14]. Phase variation characteristics of the electromagnetic bandgap structure was utilized to arrange the structure in an alternating checkerboard pattern [15]. The direction of the radar target scattering field was thus changed, and RCS was reduced.

Since digital metasurface was proposed in 2014 [16], it has been developed rapidly due to the flexible and efficient control capabilities. Digital encoded metasurface was composed of a limited number of metasurface units and can control electromagnetic waves in a discrete manner, which greatly promote

* Corresponding authors: Rui Xi (xirui@xidian.edu.cn); Lan Lan (lanlan@xidian.edu.cn); Guisheng Liao (liaogs@xidian.edu.cn).
† These authors contributed equally to this work.

beam manipulation performance. A bias network application method was proposed for two-dimensional beam scanning liquid crystal reflective phased array in 2019 [17]. First, in terms of stealth, an airborne amphibious stealth cloak was proposed that maintained efficient stealth capabilities through spatiotemporal dynamic control and random evolutionary learning algorithms [18]. In addition, it can also be applied to communication radar systems. The wireless network communication system architecture was proposed by adding a binary frequency shift keying (BFSK) communication system [19]. A theoretical framework was proposed for generating and controlling frequency modulated continuous waves (FMCWs) based on space-time coding (STC) metasurfaces, which can partially replace the radio frequency (RF) front end of traditional communication and radar systems [20]. Multi-bit coding was utilized to control the reflected beam of the metasurface [21] with the measured beam scanning capability of the entire array surface as $\pm 60^\circ$ and the gain as 19.8 dBi. A 10240-scale large-scale metasurface composed of subarrays was presented with a gain of 37.4 dBi and a beam scanning capability of $\pm 80^\circ$ [22]. A 2-bit digital coded metasurface antenna based on the convolution operation of coded metasurface was proposed [23], which had good beam deflection and multi-beam radiation performance. A digital metasurface reflector array was proposed to achieve $\pm 50^\circ$ beam pitch scanning at 12.5 GHz, with good beam scanning performance in the range of 11.75 to 13.25 GHz and a maximum aperture efficiency of 17.9% [24]. An effective beam scanning (EBS) scheme was proposed to estimate the departure angle (AoD) of the signal and improve positioning accuracy [25]. A Physics-Informed Neural Network (PINN) based method of combining neural networks with metasurfaces was proposed [26] to obtain the required directional beam with synthesized efficiency and accuracy. A deep learning-assisted method was proposed to optimize the S parameters of the metasurface [27], and the experiment demonstrated the beam forming at different angles through a certain arrangement.

Encoding the space-time coding matrix through multiple channels [28], digital messages can thus be directly transmitted to different users at different locations at the same time, realizing spatial multiplexing and frequency multiplexing at the same time. The concept of time division multiplexing metasurface (TDMM) was proposed to achieve simultaneous conversion of polarization and frequency [29]. A new space-time coding metasurface (STCM) was proposed to independently and accurately synthesize the phase and amplitude of various harmonics [30], overcoming the problem of strong entanglement of multiple harmonics. A space-division multiplexing wireless communication system with amplitude-phase independent coding based on a reconfigurable metasurface was proposed [31]. By designing dual beams with different power intensity ratios, dual channels that allow independent amplitude modulation are established. Spatial multiplexing schemes were applied to increase the number of operation wavelengths [30]. Ref. [32] proposed a multiplexing technology based on time-space modulation metasurface, which only requires one antenna to achieve multi-signal transmission. A design strategy capable of using plane waves as the incident signal is introduced to perform optical logic operations via a diffractive neural network, and three logic operations (NOT, OR, and AND) are experimentally demonstrated [33].

This paper introduces a spatiotemporal encoding method based on the digital states of different bit metasurfaces to achieve beam steering. The method involves time-modulated phase switching of metasurface units, which generates energy scattering of harmonic frequencies through reflection, and the frequency difference between these harmonics is inversely proportional to the modulation period. Through time modulation, the beam energy is distributed on the center frequency and harmonic frequencies, achieving spectrum transfer. By controlling the phase switching, the metasurface can suppress or enhance the energy scattering at specific harmonic frequencies. The proposed 1-bit switching is also inspired by checkerboard-arranged metasurface [15], which alternates the phase by setting the duty cycle to 50% of the period to form an absorber. To optimize energy scattering at harmonics, the objective function is developed by combining genetic algorithm (GA) with a primitive binary optimization method of binary particle swarm optimization (BPSO). The improved optimization method ensures the gain difference of side-lobe to main-lobe to maintain below 10 dB, while effectively increasing the main-lobe gain to 20 dBi. The metasurface is arranged with alternating reflection frequencies in a linear array to facilitate multi-beam steering. The simulation results show that it is possible to generate multi-beam far-field radiation patterns with equal distances and different angles, and beams with the same angle but different distances. Target detection at different distances at the same angle can effectively improve the accuracy of target positioning, which is particularly important in target identification. Target detection at different angles at the same distance focuses on the directional identification and spatial distribution of the target. By scanning different angles, the direction of the target can be accurately determined, thereby improving the accuracy of target positioning, and it can effectively distinguish targets with different directions but the same distance. This method is particularly important for large-scale detection, because by changing the scanning angle, a wider area can be covered. The method extends previous research by combining time-modulated metasurface coding with advanced optimization techniques to significantly improve beamforming and object detection capabilities.

2. PRINCIPLE OF SPACE-TIME MATRIX DIGITAL METASURFACE

The spatiotemporal encoding strategy can simultaneously control the spatial propagation of electromagnetic waves and the energy distribution at harmonic frequencies. Assuming that a digital metasurface consists of a two-dimensional array ($M \times N$ elements), and each element is excited with a digital state. The reflection coefficient of the element can be dynamically controlled with discrete phase or amplitude states. For the 1-bit encoding case, the reflection phase or amplitude of each element is periodically switched according to the digital spatiotemporal encoding matrix on the right of Figure 1(a). The yellow represents "1" state, and the remaining states represent "0". "1" represents amplitude value as 1, and "0" represents amplitude

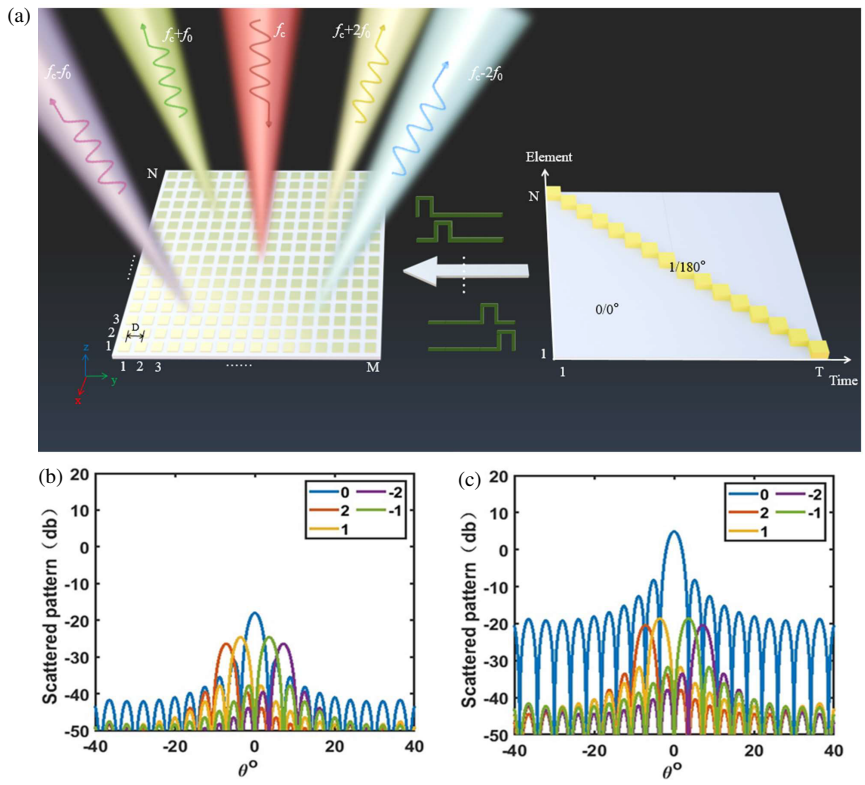

FIGURE 1. Schematic diagram and energy analysis of space-time coded metasurface reflection. (a) Space-time matrix arrangement; (b) Amplitude modulation; (c) Phase modulation.

value as 0 for amplitude modulation element, while "1" represents phase value as 180 deg, and "0" represents phase value as 0 deg for phase modulation element. Consider a single tone signal with frequency f_c incident in the normal direction on the metasurface. The time-domain far-field pattern of space-time coded scattering is defined as [16]:

$$f(\theta,\varphi,t)=\sum_{m=1}^{N}\sum_{n=1}^{N}E_{mn}(\theta,\varphi)\,\Gamma_{mn}(t)\cdot\exp\left\{-i\frac{2\pi}{\lambda_c}D\sin\theta\left\{[(n-1)\cos\varphi+(m-1)\sin\varphi]\right\}\right\}\quad(1)$$

in which $\Gamma_{mn}(t)=\sum_{l=1}^{L}A_{mn}\exp(j\varphi_{mn})U(t)$ is the time modulation reflection coefficient of the (m,n)th array element, and $U(t)$ is:

$$U(t)=\begin{cases}1 & (l-1)\tau\le t<l\tau\\ 0 & \text{other}\end{cases}\quad(2)$$

where $E_{mn}(\theta,\varphi)$ is the scattering pattern of the electromagnetic element of metasurface, which can be approximately expressed as $\cos\varphi$. λ_c is incident frequency wavelength, and $D=\lambda_c/2$ is the element spacing. θ is the azimuth angle, φ the elevation angle, N the element number in one column, and the metasurface consists of $N\times N$ elements. To transform it into the frequency domain, it needs to be Fourier transformed. Firstly, Fourier transform is performed to obtain:

$$c_{mn}^{kl}=\frac{1}{T_0}\int_0^{T_0}U(t)\exp(-j2\pi kf_0t)\,dt\quad(3)$$

The Fourier series coefficients of the periodic function can be expressed as:

$$\begin{aligned}\Phi_{mn}^{k}&=\sum_{l=1}^{L}A_{mn}\exp(j\varphi_{mn})\int_0^{T_0}U(t)\exp(-j2\pi kf_0t)\,dt\\&=\sum_{l=1}^{L}A_{mn}\exp(j\varphi_{mn})\int_{(l-1)\tau}^{l\tau}U(t)\exp(-j2\pi kf_0t)\,dt\\&=\sum_{l=1}^{L}\frac{A_{mn}\exp(j\varphi_{mn})}{L}\mathrm{sinc}\left(\frac{\pi k}{L}\right)\exp\left[\frac{-j\pi k(2l-1)}{L}\right]\end{aligned}\quad(4)$$

Through Fourier transform, the far-field scattering pattern of the space-time-coding digital metasurface at the kth harmonic frequency $f_m=f_c+kf_0(k=0,\pm1,\pm2,...)$ is written as:

$$F_k(\theta,\varphi)=\sum_{m=1}^{N}\sum_{n=1}^{N}E_{mn}(\theta,\varphi)\cdot\exp\left\{-i\frac{2\pi}{\lambda_c}D\sin\theta\left\{[(n-1)\cos\varphi+(m-1)\sin\varphi]\right\}\right\}$$

$$\sum_{l=1}^{L} \frac{A\exp\left(j\varphi_{mn}\right)}{L}\mathrm{sinc}\left(\frac{\pi k}{L}\right)\exp\left[\frac{-j\pi k\left(2l-1\right)}{L}\right] \quad (5)$$

where L is the time series length.

By introducing spatiotemporal modulation into the metasurface, it can be observed from formula (5) that the reflected beam from the metasurface not only has one beam operating at the center frequency, but also generates multiple beams operating at harmonic frequencies. The frequency difference between two adjacent harmonic frequencies is determined by the time modulation period. This concept is similar to frequency division multiplexing (FDM), a technique in which different signals are transmitted simultaneously on separate frequency bands [29]. Here, the harmonic frequencies generated by the metasurface correspond to different frequency bands, with each harmonic representing a unique signal in a manner akin to how FDM works in communication systems. Assume that the number of metasurfaces is $M \times N(M = N = 16)$, and the incident frequency is $f_c = 11\,\mathrm{GHz}$. When the space-time coding matrix is arranged as shown in Figure 1(a), each column of the metasurface shares the same state. Each column of metasurface is powered in the "1" state for AM or PM in turn within one time period, while the time period is set as T (assuming $T = 16$ here) time slices. Within the 16 time slices, 16 rows of the metasurface are stimulated in sequence. Since time sequence is introduced in AM and PM, multi-beams pointing to different directions are thus generated at different harmonic frequencies $(f_m, m = 0, \pm1, \pm2)$, as shown in Figures 1(b), (c). The amplitude generated by PM has a higher gain than AM at the center frequency f_0, and the gain of each harmonic is also higher than that of AM. Beams generated at different harmonic frequencies point to different angles, which is closely related to space division multiplexing (SDM) [30], a technique that enables multiple signals to be transmitted simultaneously by utilizing different spatial channels. In SDM, signals are separated in space, typically by using multiple antennas or directional beams, allowing them to be transmitted on the same frequency band without interference. The ability of metasurface to manipulate the direction and amplitude of each reflected beam at different harmonic frequencies enables multi-beam control. Beam generated at each harmonic frequency corresponds to a beam pointing to a distinct direction, akin to how SDM works by allocating different spatial paths for different signals.

Setting the incident angle θ as 0° and substituting it into Equation (5), the scattered energy of all harmonic components exhibits significant attenuation. The spatial phase term $\exp\left\{-i2\pi/\lambda_c D\sin\theta\left\{\left[(n-1)\cos\varphi+(m-1)\sin\varphi\right]\right\}\right\}$ in Equation (5) degenerates to 1, rendering the array's scattering properties solely dependent on the temporal coding sequence. In the implemented 1 bit coding scheme, adjacent coding elements manifest a π phase difference. Consequently, the scattered field at $\theta = 0^\circ$ is reduced to:

$$f\left(\theta\right) = \sum_{n=1}^{N} A_n \exp\left(j\varphi_n\right) = \sum_{n=1}^{N} A_n\left(-1\right)^n \quad (6)$$

This mathematical Equation (6) explicitly demonstrates that the destructive interference dominates when the spatial phase modulation becomes ineffective. The temporal coding-induced phase cancellation mechanism predominates, culminating in substantial reduction of the total scattered field intensity in the broadside direction.

The above is an analysis of the space-time matrix when it is 1-bit coded, and the beam phase is:

$$\Phi = \sum_{l=1}^{L} \frac{\Gamma_{mn}^{n}}{L}\mathrm{sinc}\left(\frac{\pi k}{L}\right)\exp\left[\frac{-j\pi k\left(2l-1\right)}{L}\right] \quad (7)$$

Calculate the cumulative phase values to get:

$$\begin{cases} \Phi_m = \sum\limits_{l=1}^{L} \frac{\Gamma_{mn}^{n}}{L}\mathrm{sinc}\left(\frac{\pi m}{L}\right)\exp\left[\frac{-j\pi m(2l-1)}{L}\right] \\ \Phi_{-m} = \sum\limits_{l=1}^{L} \frac{\Gamma_{mn}^{n}}{L}\mathrm{sinc}\left(\frac{-\pi m}{L}\right)\exp\left[\frac{j\pi m(2l-1)}{L}\right] \end{cases} \quad (8)$$

The initial phase usually takes two values, $\exp(j\pi) = -1$ and $\exp(j\cdot 0) = 1$. So we can get:

$$\Phi_m = \Phi_{-m}^{*} \quad (9)$$

Since the cumulative phase values have a conjugate relationship, when they are substituted into the energy calculation formula $F_k(\theta,\varphi)$:

$$F_{k1}\left(\theta,\varphi\right) = F_{k2}\left(-\theta,\varphi\right) \quad (10)$$

The symmetry of the beam direction is proved. The phases generated by the $+m$th harmonic and $-m$th harmonic are gradually symmetrical, so the harmonic beam pointing must be symmetrical, and the adjustability of the beam has certain limitations.

Then, the increase in bit number is analyzed. So we analyze 2-bit coding to analyze the beam. In 2-bit encoding, "0" represents $\varphi = 0^\circ$; "1" represents $\varphi = 90^\circ$; "2" represents $\varphi = 180^\circ$; "3" represents $\varphi = 270^\circ$, and bring them into the calculation of the reflection phase of the array element:

$$\exp\left(j\varphi\right) = \begin{cases} 1, & \varphi = 0^\circ \\ -j, & \varphi = 90^\circ \\ -1, & \varphi = 180^\circ \\ j, & \varphi = 270^\circ \end{cases} \quad (11)$$

Due to the additional introduction of j and $-j$ phases, the calculation of the cumulative phase is $\Phi_m \neq \Phi_{-m}^{*}$, breaks the conjugation, so the 2-bit beam controllability is high.

Then, the influence of different bit time series on harmonic distribution under PM modulation is systematically analyzed, as shown in Figure 2. The results show that the energy at the harmonic frequency breaks the inherent symmetry under PM modulation relative to the center frequency.

Assuming that the metasurface consists of $M \times N(M = N = 8)$ elements, when the incident wave is irradiated along the normal direction, assuming that the incident frequency is $f_c = 10\,\mathrm{GHz}$, and the unit spacing is half of the wavelength at the incident frequency $D = \lambda_c/2$, $L = 2$, the

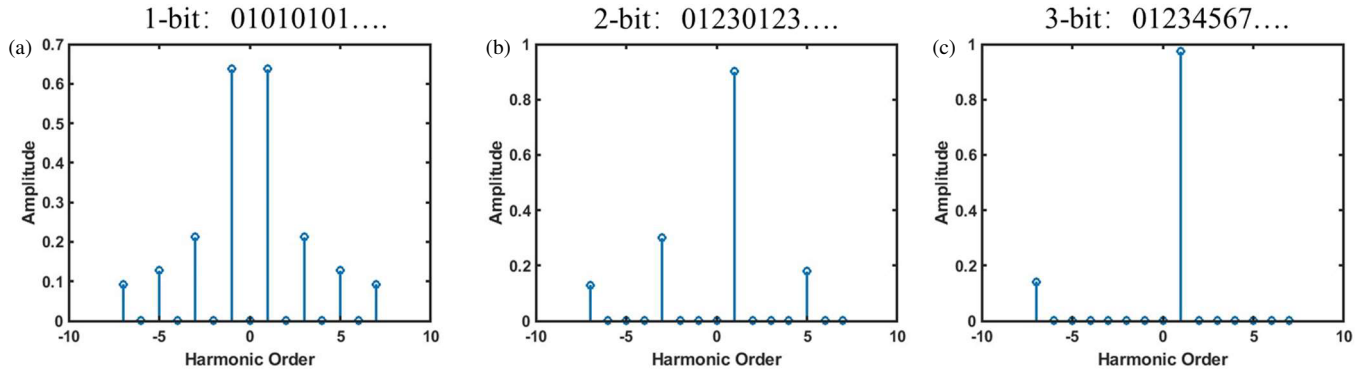

FIGURE 2. Harmonic distribution of different coding bits under PM modulation.

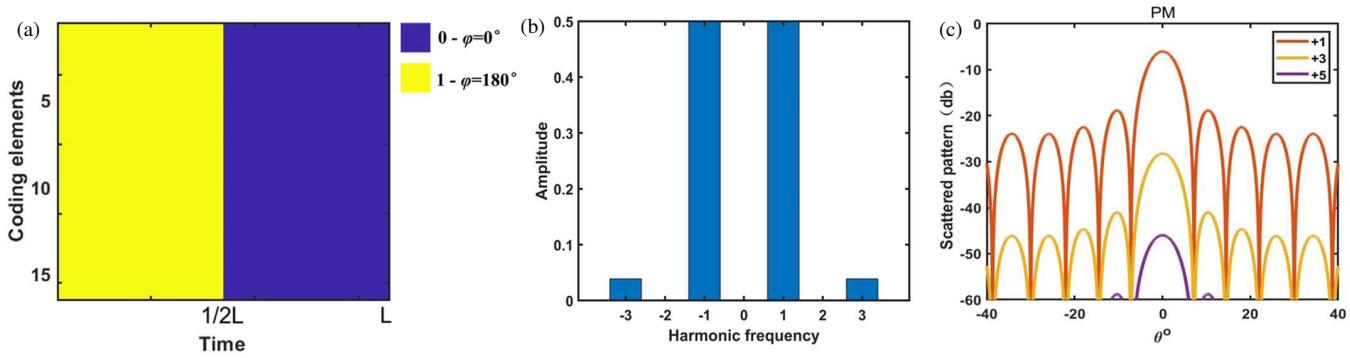

FIGURE 3. Simulation with a duty cycle of 50%. (a) Duty cycle 50% space-time matrix; (b) Harmonic energy scattering; (c) Angular scattering energy diagram.

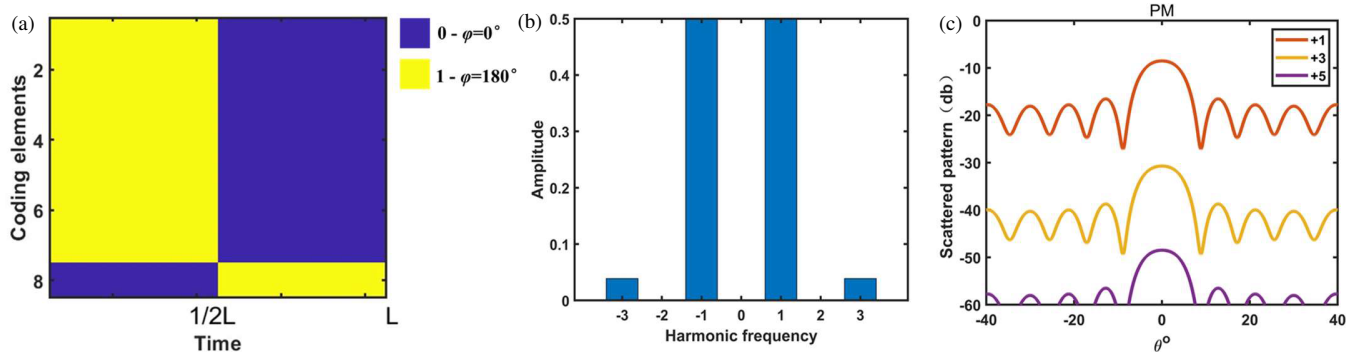

FIGURE 4. When the duty cycle is 50%, one column is oppositely excited. (a) Duty cycle 50% space-time matrix; (b) Harmonic energy scattering; (c) Angular scattering energy diagram.

energy expression can be obtained as follows:

$$f(\theta,t)=\sum_{n=1}^{N}\exp\left\{j\left(\frac{2\pi}{\lambda_c}(n-1)D\sin\theta\right)\right\}$$
$$\left[\Gamma_n^1\left(e^{-j2\pi m}-1\right)+\Gamma_n^2\left(e^{-j2\pi m}-e^{-j2\pi m\frac{1}{2}}\right)\right] \quad (12)$$

where Γ_n^1 represents the reflected phase at the $(n-1)\tau < t \leq n\tau$, $n=1,2,3,\cdots$; Γ_n^2 represents the reflected phase at the $n\tau < t \leq (n+1)\tau$, $n=1,2,3,\cdots$; m is the harmonic order.

As shown in Figure 3(a), we use 1 bit phase modulation (PM) and assume the duty cycle as 50%. The simulation results are shown in Figures 3(b) and (c), which show that for the case of duty cycle $T/2$ (50%), phase modulation exhibits selective absorption of the scattering at center frequency. This phenomenon can be attributed to the change in spatial frequency distribution caused by the time coding element, where the 50% duty cycle produces a unique phase interference pattern that can selectively obtain only odd harmonics, proving its effectiveness in absorbing scattering at even harmonics and center frequency. These findings indicate that time coding with a specific duty cycle can be used for customized energy distribution manipulation, especially for applications that require frequency selective absorption.

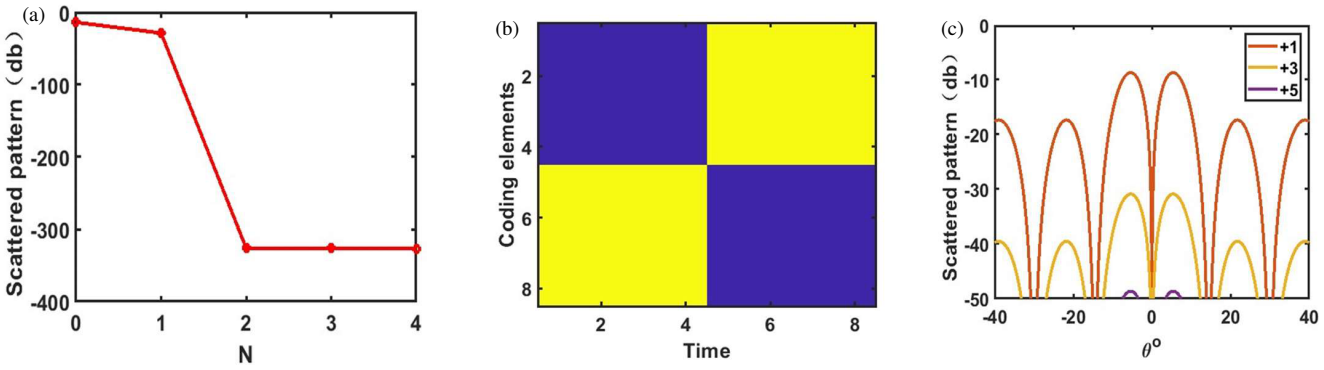

FIGURE 5. Relationship between gain and number of oppositely excited array elements. (a) Relationship between +1st harmonic boresight gain and number of oppositely excited array elements; (b) Space-time matrix; (c) Angular scattering energy diagram.

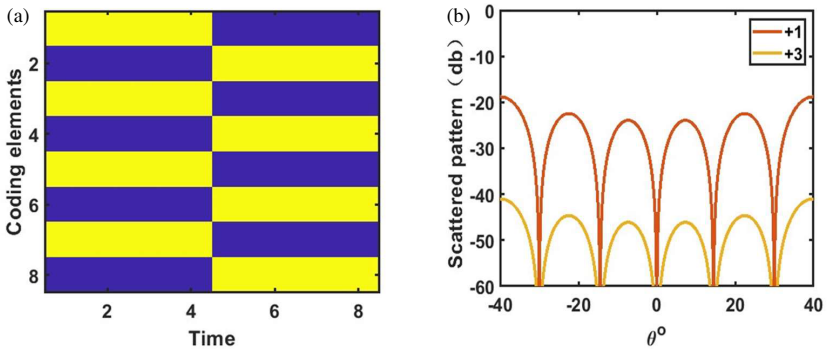

FIGURE 6. Alternately excite the opposite number of array elements. (a) Space-time matrix; (b) Angular scattering energy diagram.

On this basis, we added an alternating switching method. Next, we analyze the obtained graph (as shown in Figure 4(c)) when the excitation state of one column of array elements is opposite to that of the other seven columns of array elements (as shown in Figure 4(a)). The simulation shows that when the excitation state of one column of array elements is opposite to that of the other seven columns of array elements, only odd harmonics can be selectively obtained (as shown in Figure 4(b)), but the main lobe gain of odd harmonics will decrease, while the gain of $+1$ harmonics is still the largest. As shown in Figure 5(a), as the number of reverse excitation columns increases, the main lobe gain of $+1$ harmonic decreases accordingly, indicating that the reflected energy moves to other frequencies. Therefore, as shown in Figure 5(b), when half of the array elements adopt opposite phases, the simulation results are shown in Figure 5(c). In the line of sight direction ($\theta = 0°$), it can be observed that there is almost no reflection of high-order harmonic energy, achieving a stealth effect, but it is found that the sidelobe gain is still large.

As shown in Figure 6(a), the specific excitation method is conducted when half of the array elements are excited at the oppositely switching excitation state, while elements are alternately and oppositely excited. In the alternating arrangement, the phase difference between adjacent units changes alternately in space, forming a more complex spatial phase distribution, this specific excitation method reduces the spatial coherence of the scattered wave. The scattering energy diagram is simulated as shown in Figure 6(b). The results show that the gain is still close to 0 at the visual axis, and more energy is dispersed in different directions, resulting in effectively suppressed side lobes. Compared with Figure 6(c), the largest side lobes are reduced by about more than 10 dB. From the perspective of Fourier transform, the alternating arrangement is equivalent to introducing a high-order frequency phase modulation in the spatial frequency domain, which causes the scattered energy to be more dispersed in space and the energy density to be lower, and can thus effectively achieve stealth effect.

This method achieves electromagnetic stealth by alternately exciting the metasurface at a duty cycle of 50%, and extremely low scattering characteristics are obtained at both the center frequency and high-order harmonics. This method reflects an important design principle of digital coded metasurfaces: by increasing the discontinuity of spatial phase, more effective scattering control can be achieved. It possesses important application prospects in the fields of military stealth and wireless communications, and provides a theoretical basis and design ideas for the development of new electromagnetic stealth technology.

3. DIGITAL CODING METHOD BASED ON GENETIC ALGORITHM TO IMPROVE BINARY OPTIMIZATION ALGORITHM

The subsequent analysis uses PM modulation technology, this section designs a BPSO-GA optimization algorithm to calculate the space-time coding matrix to improve the gain of the metasurface reflection beam. The specific algorithm flowchart is shown in Figure 7.

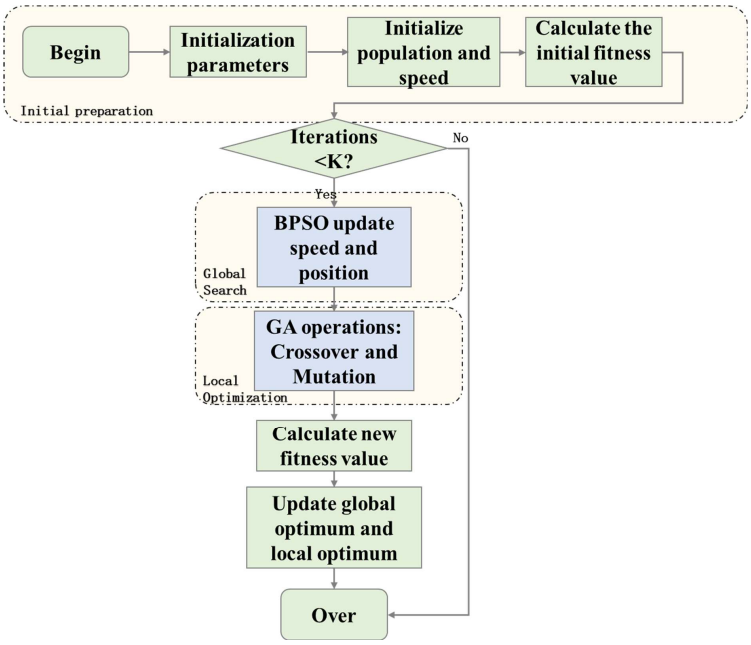

FIGURE 7. BPSO-GA algorithm flow chart.

In a digital metasurface, units with discretized digital phase states are distributed in the discrete space of the metasurface aperture. A BPSO algorithm is proposed to optimize the digital coding metasurface [34]. This paper uses the optimization algorithm to optimize the arrangement of the space-time coding matrix. The particles in the algorithm are represented by binary codes, and each array metasurface unit represents a particle. The particle velocity represents the probability of the particle position changing and determines the search direction and search distance of the particle to find the next position:

$$\begin{aligned} v_{id} &= \omega v_{id} + c_1 \text{rand1}\left(\right)\left(p_{id} - x_{id}\right) \\ &\quad + c_2 \text{rand2}\left(\right)\left(p_{gd} - x_{id}\right) \end{aligned} \tag{13}$$

where ω is the inertia weight; c_1, c_2, ω use adaptive weights and adaptive learning factors to speed up the convergence of the algorithm and improve the convergence accuracy of the algorithm.

Through formula (14), the value of the speed is mapped to the interval $\{0, 1, 2, 3\}$, so that the speed is expressed as the probability of the binary bit taking 00, 01, 10, 11. The mapping method generally uses the sigmoid function:

$$S\left(v_{id}\right) = \frac{1}{1 + \exp\left(-v_{id}\right)} \tag{14}$$

In the above formula, $S(v_{id})$ represents the probability that x_{id} takes 0, 1, 2, 3. The particle changes its position through formula:

$$x_{id} = \begin{cases} 0, & S\left(v_{id}\right) \leq 0.25 \\ 1, & S\left(v_{id}\right) \leq 0.5 \\ 2, & S\left(v_{id}\right) \leq 0.75 \\ 3, & \text{otherwise} \end{cases} \tag{15}$$

In order to prevent $S(v_{id})$ from being too close to 1 or 0, parameter $v_{\max}$ is used as the maximum speed limit value to limit the range of v_{id}, that is, $v_{id} \in [-v_{\max}, v_{\max}]$.

As a heuristic optimization algorithm, the core operations of GA include crossover and mutation, which mainly provide global random search and gene recombination. By combining the crossover and mutation operations of GA to enhance population diversity, the BPSO algorithm is prevented from falling into local optimality, and the search efficiency in high-dimensional discrete space is improved.

The crossover operation simulates the gene recombination process in biological inheritance. For two parent individuals X_1 and X_2, the single-point crossover operation can be expressed as:

$$\begin{cases} X_1 = \left[x_{11}, x_{12}, x_{1k}, x_{1(k+1)}, ..., x_{1n}\right] \\ X_2 = \left[x_{22}, x_{22}, x_{2k}, x_{2(k+1)}, ..., x_{2n}\right] \end{cases} \tag{16}$$

After selecting the crossover point k, the resulting offspring Y_1 and Y_2 can be expressed as:

$$\begin{cases} Y_1 = \left[x_{11}, x_{12}, x_{1k}, x_{2(k+1)}, ..., x_{1n}\right] \\ Y_2 = \left[x_{22}, x_{22}, x_{2k}, x_{1(k+1)}, ..., x_{2n}\right] \end{cases} \tag{17}$$

The mutation operation maintains population diversity by randomly changing certain gene positions of individuals. For the discrete value range $[0, 1, 2, 3]$, assume that the population before mutation is:

$$X = \left[x_1, x_2, x_i, ..., x_n\right] \tag{18}$$

During the mutation operation, P_m is the mutation probability, usually 0.1, and the mutated probability changes the value

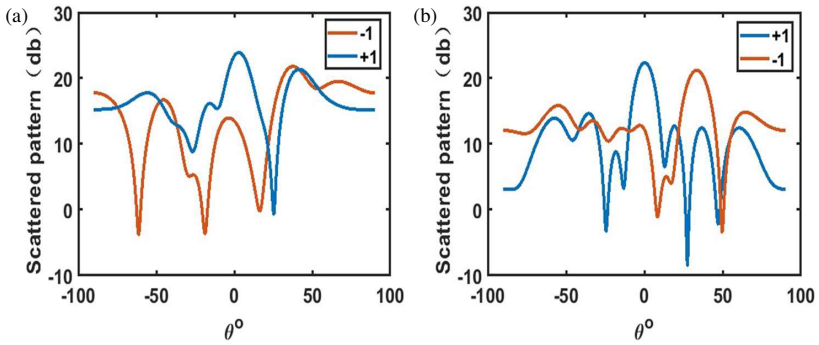

FIGURE 8. Comparison before and after algorithm optimization. (a) Before BPSO algorithm optimization. (b) After BPSO-local optimization algorithm optimization.

of a particle in the population:

$$x'(i) = \begin{cases} \text{rand}\{0,1,2,3\}, & \text{if rand}(0,1) < P_m \\ x(i), & \text{otherwise} \end{cases} \quad (19)$$

$X(i)$ represents the gene value at the ith position, and $X'(i)$ is the gene value after mutation. The population obtained after mutation is:

$$X' = \left[x_1, x_2, x_i^{'}, ..., x_n\right] \quad (20)$$

An important signal performance indicator is the side lobe level (SLL). Low side lobe level helps reduce signal interference and improve communication quality. SLL is the ratio of the side lobe peak to the main lobe maximum, generally referring the first side lobe level next to the main lobe:

$$\text{SLL} = 20\log\left(\frac{F_s(\theta)}{F_{\text{total}}(\theta)}\right) \quad (21)$$

where $F_s(\theta)$ is the side lobe energy, and $F_{\text{total}}(\theta)$ is the main peak energy.

The STC matrix is optimized with the constraints of pointing to the specified azimuth angle and peak sidelobe ratio at a specific harmonic frequency. First, the STC matrix is globally searched using the BPSO algorithm, and its fitness function is as follows:

$$\begin{aligned} \text{Fitness} = {} & w_1\left[\left(\left|\theta_s^{-1} - \theta_d^{-1}\right| + \left|\theta_s^{+1} - \theta_d^{+1}\right|\right)^2\right] \\ & + w_2\left[\left(\left|\text{SLL}_{\max}^{\pm 1} - \text{SLL}_d\right|\right)^2\right] + w_3\left(\text{SLL}_\sigma^{+1} + \text{SLL}_\sigma^{-1}\right) \end{aligned} \quad (22)$$

where $\theta_s^{\pm 1}$ is the actual beam main lobe pointing angle, $\theta_d^{\pm 1}$ the ideal beam main lobe pointing angle, w_1 the angle weight, $\text{SLL}_{\max}^{\pm 1}$ the actual beam side lobe, SLL_d the ideal beam side lobe, w_2 the side lobe weight, and $\text{SLL}_\sigma^{\pm 1}$ the side lobe uniformity limit, which is the standard deviation between the side lobes of each beam.

Each updated particle swarm is brought into the STC matrix to calculate its main lobe pointing and side lobe energy. The main lobe pointing and side lobe energy of the matrix, along with the expected mainlobe pointing and side lobe energy are all substituted into the fitness function calculation formula. The smaller the fitness function value is, the more it meets expectations.

The BPSO algorithm is used to perform a global search on the STC matrix, and then the GA is used for local search. When the global search stage reaches a certain number of iterations, or the quality of the solution found by the local search is high, it can be switched to the local search stage for refinement optimization. Finally, the elite retention strategy is adopted to directly substitute the matrix particles with the lowest fitness function in the current randomly generated STC matrix into the next generation, thereby improving the convergence speed and solution quality of the BPSO algorithm.

We assume that the desired beam -1 order points to $30°$, and $+1$ order points to $0°$, that is $\theta_d^{-1} = 30°$ and $\theta_d^{+1} = 0°$, as shown in Figure 8. The results obtained by the optimized BPSO algorithm are compared with those before the BPSO algorithm is optimized. It is found that although the beam pattern before optimization can obtain a higher main lobe, the side lobe is also relatively high, and the distinction from the main lobe beam is not obvious. In addition, the side lobe of the $+1$ harmonic is slightly higher than the main lobe of the -1 harmonic. The results of the BPSO-GA optimization algorithm are shown in Figure 8(b). While the main lobe gain is enhanced, the overall side lobe is reduced. The difference between the main lobe and side lobe is about 10 dB, and there is a clear distinction. The optimized $+1$ and -1 orders may be more concentratedly pointed to $0°$ and $30°$.

Assuming an $M \times N(M = N = 8)$ array with a modulation time period of $T = 8$, each column shares a state. "00" represents $\varphi = 0°$; "01" represents $\varphi = 90°$; "10" represents $\varphi = 180°$; and "11" represents $\varphi = 270°$. The incident frequency is $f_c = 10\,\text{GHz}$. According to the BPSO-GA algorithm, the target sample matrix is generated, and the maximum number of iterations is set as 200. Figures 9(a) and 9(g) show the fitness curve change diagram. It can be seen from the fitness curve diagram that it converges after about 50 iterations. Set the $+1$st harmonic main lobe pointing to $0°$ and the -1st harmonic main lobe pointing to $20°$. The sample matrix obtained by the algorithm is shown in Figure 9(b), and the generated beam pattern is shown in Figure 9(c). The main lobe gain can reach more than 20 dBi. Figures 9(d) and 8(e) represent the 2D far-field scattering diagrams of the -1st harmonic and $+1$st harmonic, respectively. Figure 9(f) represents its 3D far-field directional scattering diagram. When the $+1$st harmonic and -1st harmonic are both set pointing to the same angle of $-10°$,

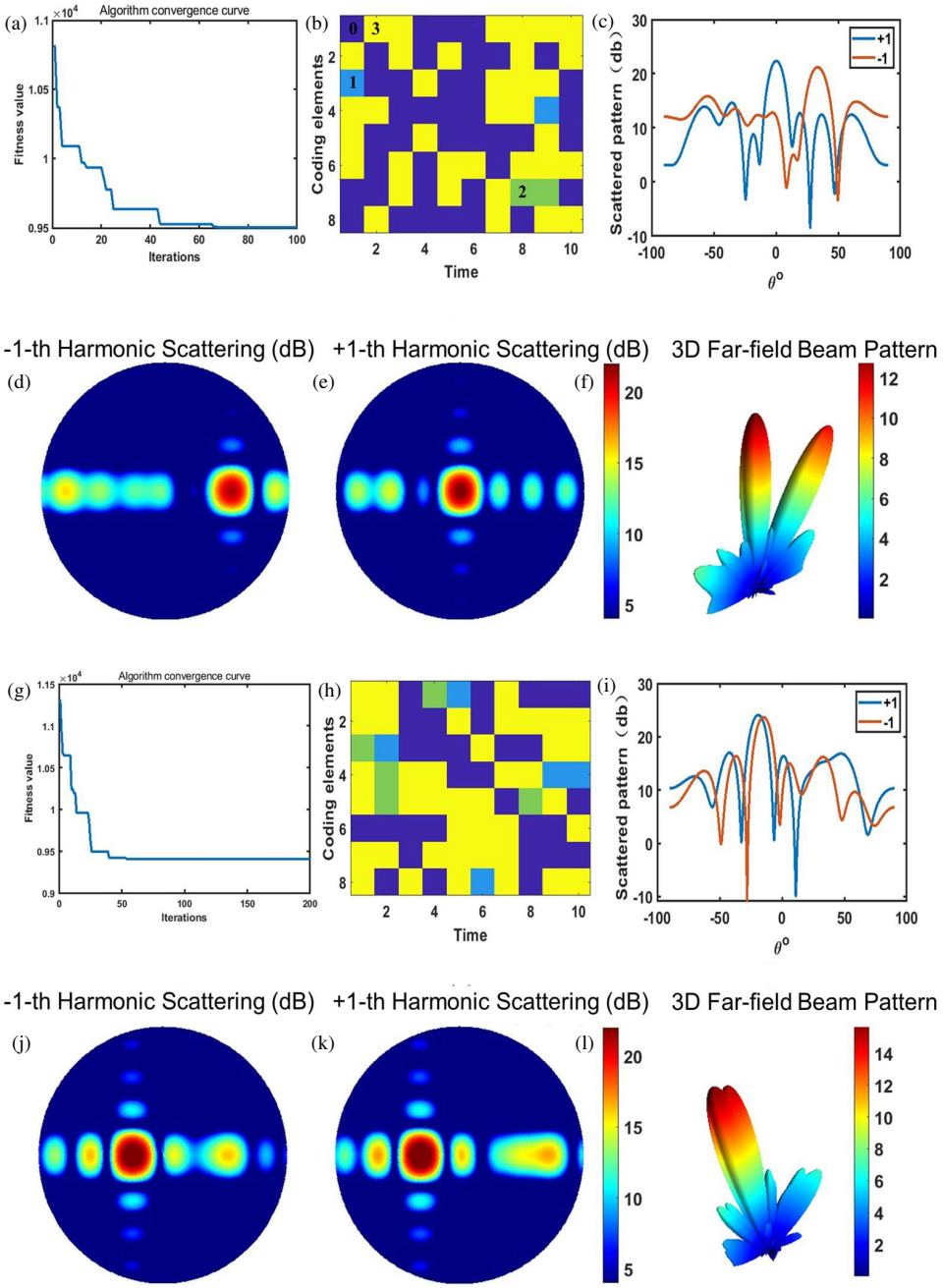

FIGURE 9. BPSO-local optimization algorithm optimized space-time matrix.

the BPSO-GA optimized STC matrix is obtained as shown in Figure 9(h), and the generated beam pattern is shown in Figure 9(i). The gain can reach 25 dBi for both harmonics, which are about 10 dB different from the side lobe. The above analysis shows that the proposed BPSO-GA optimization algorithm can achieve good suppression of the side lobes while maintaining high gain of the main lobe. Figures 9(j), (k) present the 2D far-field scattering diagrams of the -1st harmonic and $+1$st harmonic, respectively, and Figure 9(l) represents its 3D far-field directional scattering diagram.

As shown in Figure 11, assuming that the radar transmission frequency is f, there are usually multiple targets to be detected at the same distance D_1. In this case, a single beam cannot detect them at the same time. If there are multiple beams at the same distance D_1 but with different pointing angles of θ_1 and θ_2, multiple target detection at the same distance and different angles can be achieved. Similarly, when the detection targets are at different distances D_2 and D_3 but at the same angle, the radar needs to be able to detect at the same angle and different distances.

According to the above space time coding metasurface reflection characteristic, a multi-frequency signal is generated and used as the emitting source. Assume that the far-field target is located at a distance of r_0 from the reference sub-metasurface, and the spacing between two adjacent sub-metasurfaces is d. As show in Figure 10, the distance between

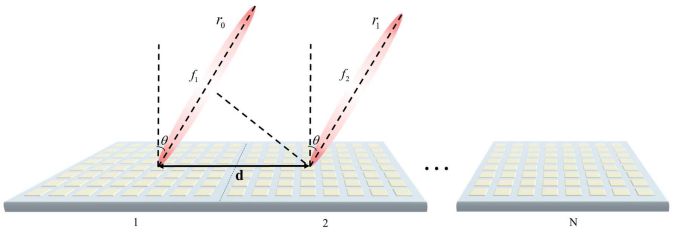

FIGURE 10. Schematic diagram of the distant target metasurface.

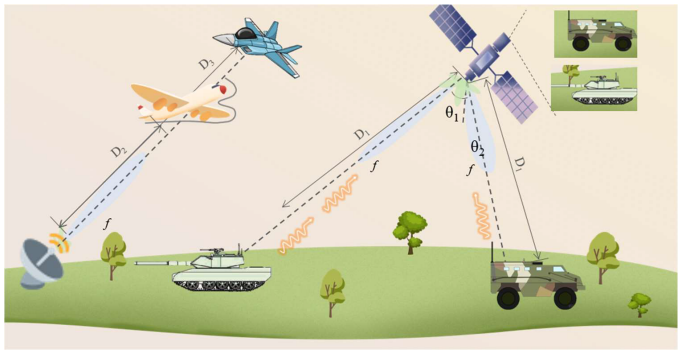

FIGURE 11. Schematic diagram of the distant target hypersurface.

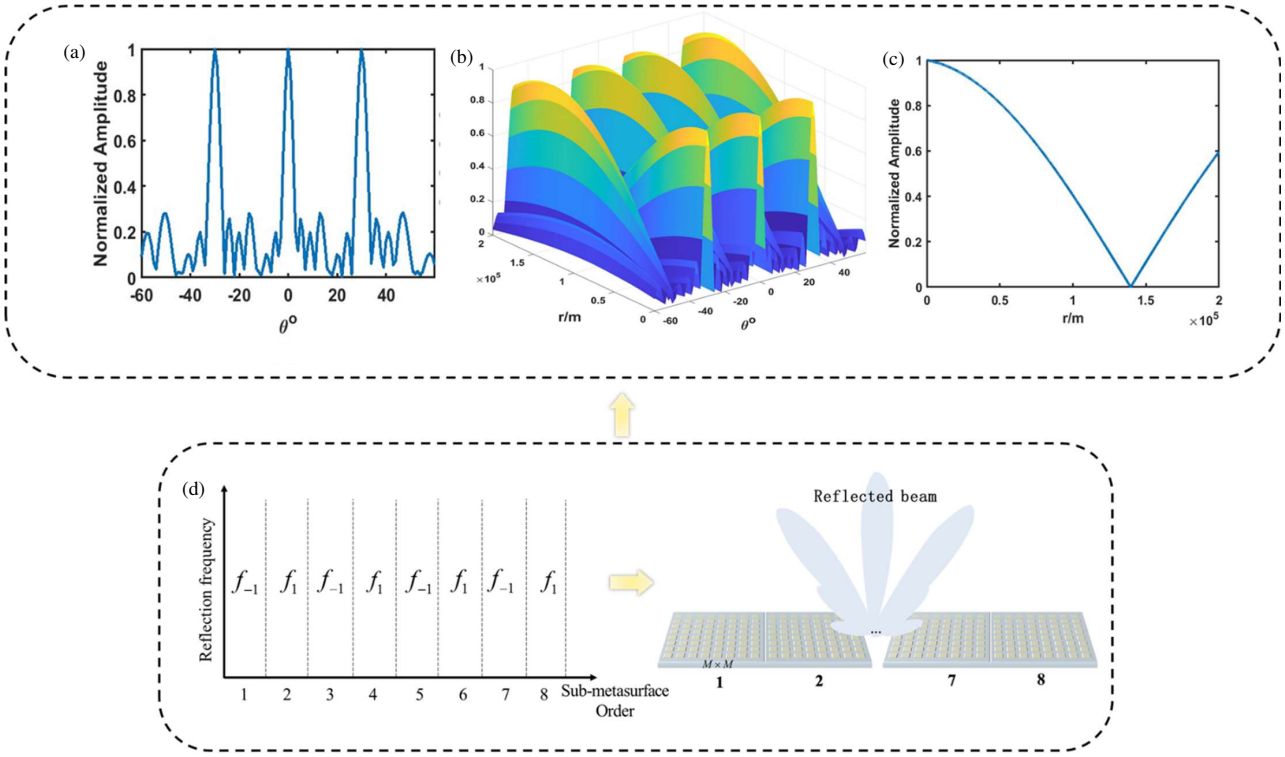

FIGURE 12. Far-field scattering and distance angle diagrams when the sub-metasurface alternate reflection frequencies. (a) Angular scattering diagram when the distance is $R = 10000$ m; (b) 3D distance angle direction diagram; (c) Distance scattering diagram when the angle is 0; (d) BPSO-GA optimizes the encoding to obtain the spatiotemporal encoding matrix.

the nth sub-metasurface and point target is:

$$r = r_0 - (n-1)\, d \sin\theta \tag{23}$$

The frequency reflected by the nth sub-metasurface is f_n. Each sub-metasurface has a certain phase and amplitude difference due to time modulation. The signal arriving at the far-field point target is:

$$s_n(t) = \exp(j2\pi f_n t) \sum_{l=1}^{L} \frac{\Gamma_n^l}{L} \operatorname{sinc}\left(\frac{\pi k}{L}\right) \exp\left[\frac{-j\pi k\,(2l-1)}{L}\right] \tag{24}$$

Then, the expression of the signal emitted by N sub-metasurface reaching the far field is:

$$\begin{aligned} & S_n\left(t - \frac{r_n}{c_0}\right) \\ &= \sum_{n=1}^{N} \frac{1}{r_n} \exp\left\{j2\pi f_n \left(t - \frac{r-(n-1)d\sin\theta}{c_0}\right)\right\} \\ & \sum_{l=1}^{L} \frac{\Gamma_n^l}{L} \operatorname{sinc}\left(\frac{\pi k}{L}\right) \exp\left[\frac{-j\pi k\,(2l-1)}{L}\right] \end{aligned} \tag{25}$$

Assume that the sub-metasurface is arrayed with $M \times N (M = N = 8)$ elements, and a total of 8 sub-

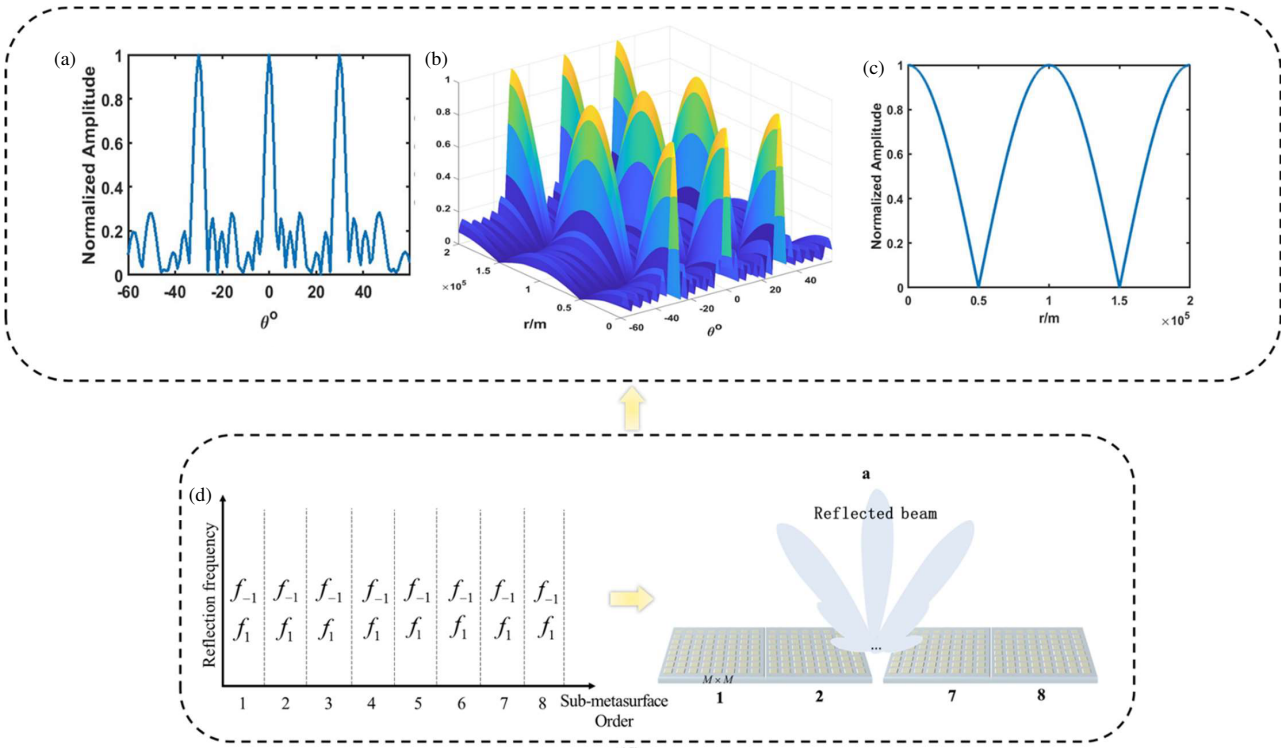

FIGURE 13. Far-field scattering and distance angle diagram when the sub-metasurface reflects two frequencies simultaneously. (a) Angular scattering diagram when the distance is $R = 10000$ m; (b) 3D distance angle direction diagram; (c) Distance scattering diagram when the angle is 0; (d) BPSO-GA optimizes the encoding to obtain the spatiotemporal encoding matrix.

metasurfaces constitutes the whole metasurface. For the first metasurface shown on Figure 12, each sub-metasurface reflects a single frequency; for the second metasurface on the right side of Figure 13, each sub-metasurface reflects dual frequencies.

As shown in Figure 12 and Figure 13, when the incident frequency is $f_c = 10$ GHz and $R = 10000$ m, the far-field energy of the metasurface under this distribution is calculated, and the angular scattering diagram of the far field $R = 10000$ m is observed. For the first metasurface shown on Figure 12, the 1st, 3rd, 5th, and 7th sub-metasurfaces reflect the -1st frequency, while the 2nd, 4th, 6th, and 8th sub-metasurfaces reflect the 1st harmonic frequency. The beam pattern of the reflected waveform at designated angle is optimized by BPSO. It is found that 3 beams are generated, as shown in Figure 12(a). The three peaks point to $-37°$, $0°$, and $37°$. Figure 12(b) shows the relationship between angle and distance. Figure 12(c) shows the relationship between gain and distance.

For the second metasurface shown on Figure 13, the sub-metasurface reflects the dual frequencies of the -1st frequency and the 1st harmonic. The angle of the reflected waveform is controlled to be consistent through the BPSO. As shown in Figure 13(a), it is found that 3 beams are generated. The three peaks also point to $-37°$, $0°$, and $37°$. Figure 13(b) shows the relationship between angle and distance. Figure 13(c) shows the relationship between beam gain and distance. However, compared with Figure 12(c), the beam in Figure 13(c) is more concentrated in the distance dimension, that is, the accuracy in the distance dimension is better, and the detection of different distances at the same angle can be achieved.

4. EXPERIMENT

We fabricated a metasurface array composed of 8×8 elements for experiment. Its total size is 112 mm $\times$ 112 mm, printed on an F4B substrate (relative permittivity $\varepsilon_r = 2.63$, tangent loss $\tan\delta = 0.001$), and the substrate thickness is 1.5 mm. The actual image of the fabricated sample is shown in the right of Figure 14. The thickness of the printed copper coating is 0.035 mm. The unit uses two pin diodes (MADP-000907-14020x from MACOM) to obtain a 90° phase difference when the two diodes switch between the 2 bit of "ON-OFF (00)", "ON-ON (01)", "OFF-OFF (10)", and "OFF-ON (11)" states.

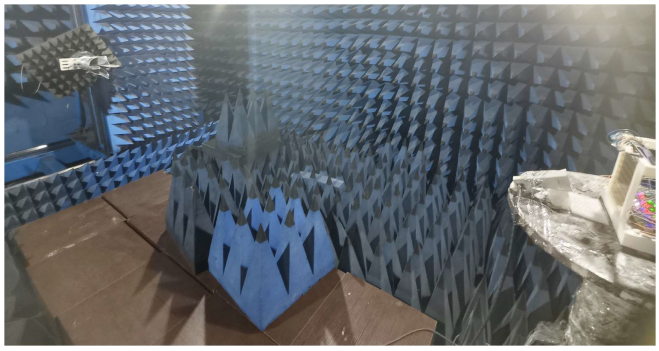

FIGURE 14. Experimental test setup.

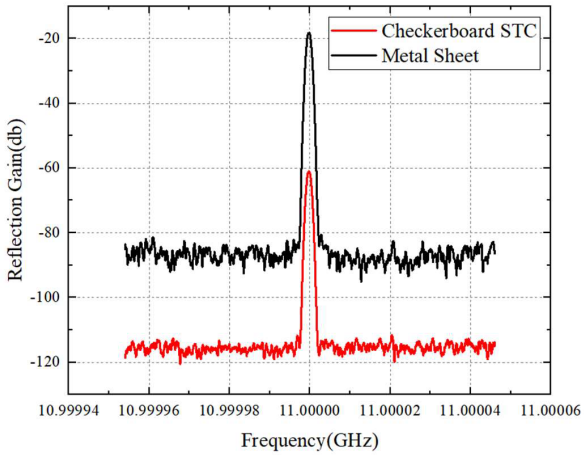

FIGURE 15. Experimental test results.

Since the metasurface needs to be coded and controlled, we use FPGA (ALINX Black Gold FPGA Development Board Xilinx Zynq Development Board 7020) for coding input and control. The experimental equipment uses a signal generator (Keysight E8267D) connected to the horn antenna to irradiate the metasurface with a monochromatic wave with a frequency of 11 GHz and uses another horn antenna as a receiving antenna, connected to a spectrum analyzer (Keysight N5230C) for receiving spectrum inspection. The specific experimental setup is shown in Figure 14. Activate the coding control system using a 50% duty cycle to switch the coding state, and the coding state is "00-10".

The experimental results are shown in Figure 15. It can be clearly seen from the spectrum that when there is no coding to control the regular reflection, the spectrum only contains the frequency of the incident wave. When the coding is switched at a duty cycle of 50%, the gain at the incident frequency is reduced, and the harmonics are also suppressed.

5. CONCLUSION

This paper presents a novel metasurface design based on space-time coding matrices, demonstrating significant advancements in beamforming and harmonic frequency control. One of the key insights gained from this work is the ability of the metasurface to absorb energy in the line of sight while simultaneously reducing side lobes when operating with a 50% duty cycle. This capability not only enhances the overall performance of the system but also enables more efficient electromagnetic wave control, crucial for applications in radar and communication systems. The integration of the Binary Particle Swarm Optimization (BPSO) algorithm with genetic principles for time modulation allows the metasurface to selectively absorb or reflect specific harmonic frequencies. This flexibility enables precise multi-beam control, facilitating the generation of far-field radiation patterns with beams that can be directed at different distances and angles. Specifically, we demonstrated that metasurfaces arranged in linear arrays can produce beams at equal distances but different angles, making them suitable for detecting targets at multiple ranges.

Furthermore, the study reveals the potential of dividing the metasurface into columns, where different regions reflect frequencies in both linear and nonlinear patterns. This configuration enables the creation of beams that focus on the same distance, leading to far-field multi-point focusing. The findings offer valuable insights into how space-time modulation of metasurfaces can be used to control both spatial and frequency domains in a highly dynamic manner.

The significance of this work lies not only in the development of a flexible and high-performance metasurface design but also in its practical implications for real-world systems. The ability to precisely manipulate harmonic frequencies and beam directionality is essential for the next generation of radar, wireless communication, and adaptive antenna systems. From a theoretical standpoint, this research contributes to the broader understanding of time-modulated metasurfaces and their potential for advanced electromagnetic wave control. Practically, it opens up new avenues for improving target detection, communication efficiency, and system scalability in complex environments, marking a significant step forward in the field of electromagnetic wave manipulation.

ACKNOWLEDGEMENT

This work was supported by the National Natural Science Foundation of China (Grant No. 61931016), the Natural Science Foundation of Zhejiang Province (No. LZ24A050002), the Fundamental Research Funds for the Central Universities and the Innovation Fund of Xdian University (No. XJSJ24094).

REFERENCES

[1] Yu, N. and F. Capasso, "Flat optics with designer metasurfaces," *Nature Materials*, Vol. 13, No. 2, 139–150, 2014.

[2] Chen, H.-T., A. J. Taylor, and N. Yu, "A review of metasurfaces: Physics and applications," *Reports on Progress in Physics*, Vol. 79, No. 7, 076401, 2016.

[3] Liu, S., T. J. Cui, Q. Xu, D. Bao, L. Du, X. Wan, W. X. Tang, C. Ouyang, X. Y. Zhou, H. Yuan, *et al.*, "Anisotropic coding metamaterials and their powerful manipulation of differently polarized terahertz waves," *Light: Science & Applications*, Vol. 5, No. 5, e16076, 2016.

[4] Chen, H., L. Ran, J. Huangfu, X. Zhang, K. Chen, T. M. Grzegorczyk, and J. A. Kong, "Left-handed materials composed of only S-shaped resonators," *Physical Review E — Statistical, Nonlinear, and Soft Matter Physics*, Vol. 70, No. 5, 057605, 2004.

[5] Yang, X. M., X. Y. Zhou, Q. Cheng, H. F. Ma, and T. J. Cui, "Diffuse reflections by randomly gradient index metamaterials," *Optics Letters*, Vol. 35, No. 6, 808–810, 2010.

[6] Lier, E., D. H. Werner, C. P. Scarborough, Q. Wu, and J. A. Bossard, "An octave-bandwidth negligible-loss radiofrequency metamaterial," *Nature Materials*, Vol. 10, No. 3, 216–222, 2011.

[7] Liu, Y. and X. Zhao, "Perfect absorber metamaterial for designing low-RCS patch antenna," *IEEE Antennas and Wireless Propagation Letters*, Vol. 13, 1473–1476, 2014.

[8] Zhao, Y., J. Gao, X. Cao, T. Liu, L. Xu, X. Liu, and L. Cong, "In-band RCS reduction of waveguide slot array using metasurface bars," *IEEE Transactions on Antennas and Propagation*, Vol. 65, No. 2, 943–947, 2016.

[9] Chen, H., B.-I. Wu, B. Zhang, and J. A. Kong, "Electromagnetic wave interactions with a metamaterial cloak," *Physical Review*

Letters, Vol. 99, No. 6, 063903, 2007.

[10] Qian, C., B. Zheng, Y. Shen, L. Jing, E. Li, L. Shen, and H. Chen, "Deep-learning-enabled self-adaptive microwave cloak without human intervention," *Nature Photonics*, Vol. 14, No. 6, 383–390, 2020.

[11] Chen, H., B. Zheng, L. Shen, H. Wang, X. Zhang, N. I. Zheludev, and B. Zhang, "Ray-optics cloaking devices for large objects in incoherent natural light," *Nature Communications*, Vol. 4, No. 1, 2652, 2013.

[12] Yang, Y., Z. Gao, H. Xue, L. Zhang, M. He, Z. Yang, R. Singh, Y. Chong, B. Zhang, and H. Chen, "Realization of a three-dimensional photonic topological insulator," *Nature*, Vol. 565, No. 7741, 622–626, 2019.

[13] Yang, Y., L. Jing, B. Zheng, R. Hao, W. Yin, E. Li, C. M. Soukoulis, and H. Chen, "Full-polarization 3D metasurface cloak with preserved amplitude and phase," *Advanced Materials*, Vol. 28, No. 32, 6866–6871, 2016.

[14] Zheng, B., H. Lu, C. Qian, D. Ye, Y. Luo, and H. Chen, "Revealing the transformation invariance of full-parameter omnidirectional invisibility cloaks," *Electromagnetic Science*, Vol. 1, No. 2, 1–7, 2023.

[15] Chen, W., C. A. Balanis, and C. R. Birtcher, "Checkerboard EBG surfaces for wideband radar cross section reduction," *IEEE Transactions on Antennas and Propagation*, Vol. 63, No. 6, 2636–2645, Jun. 2015.

[16] Cui, T. J., M. Q. Qi, X. Wan, J. Zhao, and Q. Cheng, "Coding metamaterials, digital metamaterials and programmable metamaterials," *Light: Science & Applications*, Vol. 3, No. 10, e218, 2014.

[17] Li, J.-X., T. Jin, D. Erni, F.-Y. Meng, Q. Wu, and W.-N. Li, "Design and numerical demonstration of a 2D millimeter-wave beam-scanning reflectarray based on liquid crystals and a static driving technique," *Journal of Physics D: Applied Physics*, Vol. 52, No. 27, 275103, 2019.

[18] Qian, C., Y. Jia, Z. Wang, J. Chen, P. Lin, X. Zhu, E. Li, and H. Chen, "Autonomous aeroamphibious invisibility cloak with stochastic-evolution learning," *Advanced Photonics*, Vol. 6, No. 1, 016001, 2024.

[19] Zhao, J., X. Yang, J. Y. Dai, Q. Cheng, X. Li, N. H. Qi, J. C. Ke, G. D. Bai, S. Liu, S. Jin, *et al.*, "Programmable time-domain digital-coding metasurface for non-linear harmonic manipulation and new wireless communication systems," *National Science Review*, Vol. 6, No. 2, 231–238, 2019.

[20] Ke, J. C., J. Y. Dai, J. W. Zhang, Z. Chen, M. Z. Chen, Y. Lu, L. Zhang, L. Wang, Q. Y. Zhou, L. Li, *et al.*, "Frequency-modulated continuous waves controlled by space-time-coding metasurface with nonlinearly periodic phases," *Light: Science & Applications*, Vol. 11, No. 1, 273, 2022.

[21] Yang, H., F. Yang, S. Xu, Y. Mao, M. Li, X. Cao, and J. Gao, "A 1-bit 10×10 reconfigurable reflectarray antenna: Design, optimization, and experiment," *IEEE Transactions on Antennas and Propagation*, Vol. 64, No. 6, 2246–2254, 2016.

[22] Pan, X., F. Yang, S. Xu, and M. Li, "A 10 240-element reconfigurable reflectarray with fast steerable monopulse patterns," *IEEE Transactions on Antennas and Propagation*, Vol. 69, No. 1, 173–181, 2021.

[23] Xu, P., W. X. Jiang, X. Cai, S. H. Bai, and T. J. Cui, "An integrated coding-metasurface-based array antenna," *IEEE Transactions on Antennas and Propagation*, Vol. 68, No. 2, 891–899, 2019.

[24] Alhafid, A. K., S. Younis, and Y. E. M. Ali, "Enhanced far-field localization scheme using multi-RIS and efficient beam sweeping," *Progress In Electromagnetics Research C*, Vol. 140, 163–175, 2024.

[25] Diaby, F., A. Clemente, R. Sauleau, K. T. Pham, and L. Dussopt, "2 bit reconfigurable unit-cell and electronically steerable transmitarray at Ka-band," *IEEE Transactions on Antennas and Propagation*, Vol. 68, No. 6, 5003–5008, 2020.

[26] Wang, P., Z. Li, Z. Wei, T. Wu, C. Luo, W. Jiang, T. Hong, G. F. Pedersen, and M. Shen, "Space-time-coding digital metasurface element design based on state recognition and mapping methods with CNN-LSTM-DNN," *IEEE Transactions on Antennas and Propagation*, Vol. 72, No. 6, 4962–4975, 2024.

[27] Li, S., Z. Liu, S. Fu, Y. Wang, and F. Xu, "Intelligent beamforming via physics-inspired neural networks on programmable metasurface," *IEEE Transactions on Antennas and Propagation*, Vol. 70, No. 6, 4589–4599, 2022.

[28] Zhang, L., M. Z. Chen, W. Tang, J. Y. Dai, L. Miao, X. Y. Zhou, S. Jin, Q. Cheng, and T. J. Cui, "A wireless communication scheme based on space- and frequency-division multiplexing using digital metasurfaces," *Nature Electronics*, Vol. 4, No. 3, 218–227, 2021.

[29] Yang, J., J. C. Ke, W. K. Cao, M. Z. Chen, Q. Cheng, V. Galdi, and T. J. Cui, "Simultaneous conversion of polarization and frequency via time-division-multiplexing metasurfaces," *Advanced Optical Materials*, Vol. 9, No. 22, 2101043, 2021.

[30] Luo, Z., Z. Zhang, J. Tai, L. Zhang, C. Gao, H. F. Ma, W. X. Jiang, Q. Cheng, and T. J. Cui, "Fully breaking entanglement of multiple harmonics for space- and frequency-division multiplexing wireless applications via space-time-coding metasurface," *Advanced Science*, Vol. 11, No. 34, 2404558, 2024.

[31] Xiong, Q., Z. Zhang, C. Huang, M. Pu, J. Luo, Y. Guo, J. Ye, W. Pan, X. Ma, L. Yan, and X. Luo, "Amplitude-phase independently encoding space-division multiplexed wireless communication using beamforming reconfigurable metasurfaces," *Advanced Optical Materials*, Vol. 12, No. 28, 2401181, 2024.

[32] Wang, X. and C. Caloz, "Spacetime-modulated metasurface for spatial multiplexing communication," in *2019 Thirteenth International Congress on Artificial Materials for Novel Wave Phenomena (Metamaterials)*, X–465, Rome, Italy, Sep. 2019.

[33] Gunawan, R., E. Winarko, and R. Pulungan, "A BPSO-based method for high-utility itemset mining without minimum utility threshold," *Knowledge-Based Systems*, Vol. 190, 105164, 2020.

[34] Qian, C., X. Lin, X. Lin, J. Xu, Y. Sun, E. Li, B. Zhang, and H. Chen, "Performing optical logic operations by a diffractive neural network," *Light: Science & Applications*, Vol. 9, No. 1, 59, 2020.